

Artificial electrostriction in composite materials

A. SINGH,* M. J. A. SMITH, AND C. MARTIJN DE STERKE

Centre for Ultrahigh bandwidth Devices for Optical Systems (CUDOS), Institute of Photonics and Optical Science (IPOS), School of Physics, The University of Sydney, Camperdown, NSW 2006, Australia

*Corresponding author: asin4210@uni.sydney.edu.au

Received 31 March 2017; revised 6 June 2017; accepted 8 June 2017; posted 14 June 2017 (Doc. ID 291865); published 10 July 2017

We examine the role of artificial electrostriction in composites comprising solid materials, extending earlier theoretical models that omit the effect of shear. We accurately describe artificial electrostriction in such materials and present results for a selection of technologically important material combinations. © 2017 Optical Society of America

OCIS codes: (160.0160) Materials; (160.1050) Acousto-optical materials; (160.4236) Nanomaterials.

<https://doi.org/10.1364/JOSAB.34.001573>

1. INTRODUCTION

Optoacoustics is a rapidly expanding field examining the relationship between electromagnetic fields and deformations of a structure. The first optoacoustic effect, piezoelectricity [1,2], is well understood and used in sensors, motors, and for power harvesting. However, piezoelectricity only occurs in materials lacking inversion symmetry. In contrast, electrostriction, the second optoacoustic effect [3,4], is the quadratic dependence of mechanical stress on the electric field. It occurs in all materials, and so affects a greater variety of technologies. It can be thought of as a change in the bond length between atoms under the influence of an applied electric field [4].

One area in which an understanding of electrostriction is important is stimulated Brillouin scattering (SBS) [5]. Classically, SBS involves a light wave propagating through a crystal exciting acoustic waves via electrostriction. This effectively creates a moving diffraction grating which backscatters the light toward the source, and shifts it to a slightly lower frequency (see Fig. 1). In a quantum framework, this process is understood as an interaction between photons and phonons, again via electrostriction. SBS features in the design of many nano-scale devices, including Brillouin lasers, sensors, and integrated photonic circuits [6], but is also considered a major problem for signal transmission in optical fibers [7]. Manipulating SBS is crucial for new nano-scale technologies, and so it is important to understand electrostriction, its underlying mechanism.

In this paper, electrostriction is defined through [3]

$$\sigma_{ij} = -\frac{1}{2}\epsilon_0\gamma_{ijkl}E_kE_l^*, \quad (1)$$

where σ_{ij} denotes the mechanical stress tensor, ϵ_0 the permittivity of free space, γ_{ijkl} the fourth-rank electrostriction tensor, and E_j the electric field. For an isotropic material under hydrostatic pressure, this reduces to the form [8,9]

$$P = -\frac{1}{2}\epsilon_0\gamma E_kE_k^*, \quad (2)$$

with γ_{ijkl} replaced by the hydrostatic electrostriction parameter

$$\gamma = \rho \frac{\partial \epsilon_r}{\partial \rho}, \quad (3)$$

where ϵ_r is the dielectric constant and with ρ representing the material density. When the assumptions of a hydrostatic response are removed, as in Sections 2.C and 2.D, no such simplification is possible.

The study of the electrostrictive properties of composite materials is relatively recent. Smith *et al.* [8] found that two hypothetical materials without electrostriction can produce a composite with non-zero electrostriction through *artificial electrostriction*. This important result implies that the electrostriction of a composite material cannot be expressed as a suitable average of the electrostriction of the constituent materials. However, the approach of Smith *et al.* is limited in scope, as it does not account for shear effects [8], while full numerical calculations [10] of the artificial term provide little insight into the underlying physics. In this work, we present a complete explanation of artificial electrostriction, with a particular focus on its consequences in optoacoustics. This allows for the future design of metamaterials with enhanced or suppressed electrostrictive properties.

We explain the mechanism for artificial electrostriction as owing to the change in shape and volume fraction of the components of a composite upon deformation. Our methods apply to composites with internal structures that are significantly smaller ($\lesssim 10\times$) than the optical wavelength. This condition means that the electric field is approximately constant over the unit cell, allowing effective permittivities to be defined.

The outline of this paper is as follows. In Sections 2.A and 2.B, we analyze an analytic model for artificial electrostriction for liquid-liquid composites [8]. As this model does not include

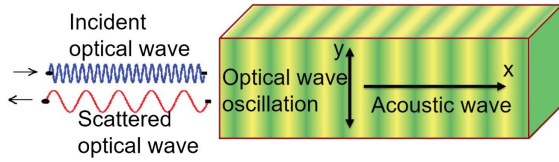


Fig. 1. Outline of conventional SBS process. We take the light to be y -polarized and propagating in the x -direction, creating a longitudinal acoustic wave propagating in x .

shear, Section 2.C examines a numerical method used to calculate the artificial electrostriction, and Section 2.D presents an alternative, semi-analytic model that can be used when shear is included. We apply our approach to technologically important materials in Section 3, and discuss these results in Section 4.

2. ELECTROSTRICTION IN COMPOSITE MEDIA

In this section, we explain the origin of artificial electrostriction in composite media. We consider composites comprising spherical inclusions in a simple cubic lattice (Fig. 2) and with isotropic constituents that are lossless and non-dispersive. We begin with a treatment of artificial electrostriction in composites with only hydrostatic pressure response, and then expand the analysis to include shear in Sections 2.C and 2.D.

A. Introduction to Zero-Shear Composites

For composites formed with shear-free media (e.g., an emulsion of two liquids), expression (3) for γ is sufficient to describe the electrostrictive properties of the mixture. We note that this simplified approach is often taken in textbooks. To evaluate the shear-free γ , we use the Maxwell–Garnett model [11,12], which gives the optical properties of composites with dilute spherical inclusions of permittivity ϵ_i embedded in an otherwise uniform matrix of permittivity ϵ_m . It takes the form

$$\epsilon_r^{\text{eff}} = \epsilon_m + \frac{3\epsilon_m(\epsilon_i - \epsilon_m)f}{(\epsilon_i + 2\epsilon_m) - (\epsilon_i - \epsilon_m)f}, \quad (4)$$

where f is the volume fraction of the inclusion in the unit cell. The appearance of factors 2 and 3 in Eq. (4) owes to the depolarization factor \mathbf{g} . The depolarization factor relates the electric field in the inclusion to that in the matrix [13,14], and depends only on the shape of the inclusion. For spheres, $\mathbf{g} \equiv (g_x, g_y, g_z) = (\frac{1}{3}, \frac{1}{3}, \frac{1}{3})$. For more general shapes, we have $0 \leq g_{x,y,z} \leq 1$ depending on the shape of the inclusion, with $g_x + g_y + g_z = 1$. For reference, an oblate spheroid centered

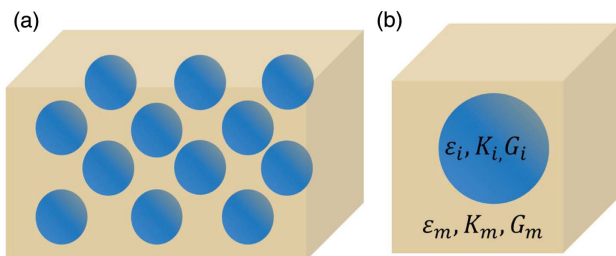


Fig. 2. (a) Diagram of lattice composed of many unit cells. (b) Single unit cell.

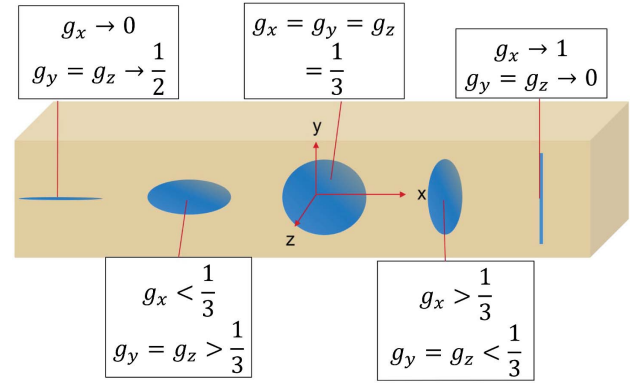


Fig. 3. Illustration of the relation between the depolarization factor \mathbf{g} and the shape of inclusion.

on the x -axis has $g_x > \frac{1}{3}$ with $g_y = g_z < \frac{1}{3}$; for a prolate spheroid, $g_x < \frac{1}{3}$ with $g_y = g_z > \frac{1}{3}$; for a plane orthogonal to the x -axis, $g_x = 1$ with $g_y = g_z = 0$; and for a needle parallel to the x -axis, $g_x = 0$ with $g_y = g_z = \frac{1}{2}$. These depolarization factors, illustrated in Fig. 3, along with the associated geometries are important for our discussion in Section 2.C, where they will be used to quantify shape changes resulting from the inclusion of shear forces.

In the absence of shear stresses, any changes in density preserve the spherical shape of the inclusion. Hence using Eqs. (4) and (3), it can be shown that [8]

$$\gamma = (\dots)\gamma_i + (\dots)\gamma_m + \gamma_{\text{art}}, \quad (5)$$

where

$$\begin{aligned} \gamma_{\text{art}} &= \rho^{\text{eff}} \frac{\partial \epsilon_r^{\text{eff}}}{\partial f} \frac{\partial f}{\partial \rho^{\text{eff}}} \\ &= \epsilon_m \left(\frac{3(\epsilon_i/\epsilon_m - 1)(\epsilon_i/\epsilon_m + 2)}{[\epsilon_i/\epsilon_m + 2 - (\epsilon_i/\epsilon_m - 1)f]^2} \right) \left(\frac{f(1-f)(K_i/K_m - 1)}{f + (1-f)K_i/K_m} \right). \end{aligned} \quad (6)$$

Here K_i and K_m are the bulk moduli of the inclusion and matrix, respectively, γ_i and γ_m are the intrinsic electrostriction parameters for the constituents, and the factors (\dots) denote functions of $K_{i,m}$ and $\epsilon_{i,m}$ [8].

Equation (5) shows that two materials with zero electrostriction, i.e., $\gamma_i = \gamma_m = 0$, can be combined to form a composite with non-zero electrostriction. This *artificial electrostriction* γ_{art} [see Eq. (6)] arises from changes in volume fraction under compression, which subsequently alters the effective permittivity of the composite, when the inclusion and matrix permittivities and bulk moduli differ. The first bracket in Eq. (6) represents $\partial \epsilon_r^{\text{eff}} / \partial f$ while the second bracket represents $\partial f / \partial \rho^{\text{eff}}$ [8]; we return to this in Section 2.B. The factor $f(1-f)$ indicates that the artificial term only exists for composites, as required. Although this model is limited in scope, it gives insight into the underlying physics. Next, we investigate the properties of γ_{art} .

B. Artificial Electrostriction in Zero-Shear Composites

In the following analysis we set $\gamma_i = \gamma_m = 0$ in Eq. (6), and thus investigate γ_{art} alone. As such, the phrases electrostriction

and artificial electrostriction are strictly equivalent in our study. Aside from an ϵ_m prefactor, γ_{art} depends only on the ratios K_i/K_m , ϵ_i/ϵ_m , and the fill fraction f . We fix f at the dilute value of $f = 0.1$ so that surface plots of γ_{art} are against the permittivity contrast $\epsilon_i - \epsilon_m$ and the ratio of bulk moduli K_i/K_m alone. These axes are chosen as the acoustic properties of materials vary much more widely compared to the optical properties.

Figure 4 is a contour plot of γ_{art} against permittivity and stiffness contrasts. We first consider the sign of the electrostriction in each region (a)–(h), and then consider the differences in its magnitude between the regions. Starting with quadrant (a), if such a composite ($\epsilon_i < \epsilon_m$, $K_i < K_m$) is compressed, the inclusion experiences a greater compression than the matrix (as $K_i < K_m$). Thus f is reduced under compression, and the composite's permittivity gains the character of the matrix. Thus ϵ_r^{eff} increases under compression by Eq. (4) (since $\epsilon_i < \epsilon_m$), so by the analog to Eq. (3), it follows that $\gamma_{\text{art}} > 0$. In quadrant (b) ($\epsilon_i > \epsilon_m$, $K_i < K_m$), the same argument applies but the permittivities are reversed, so $\gamma_{\text{art}} < 0$. In quadrant (c) ($\epsilon_i < \epsilon_m$, $K_i > K_m$), we consider the reverse of the argument applied to (a). Now the matrix has the lower bulk modulus, so f increases under compression. Since the inclusion has the lower permittivity, the effective permittivity is reduced, so $\gamma_{\text{art}} < 0$. In quadrant (d), the permittivities are switched, so $\gamma_{\text{art}} > 0$. Finally, along the line (e)–(f) $\gamma_{\text{art}} = 0$ as $K_m = K_i$, and along the line (g)–(h) $\gamma_{\text{art}} = 0$ as well, as $\epsilon_m = \epsilon_i$.

We now consider the magnitude of the electrostriction in these regions. First, γ_{art} is larger in magnitude on the left of Fig. 4 than on the right. This asymmetry owes entirely to the fact that $f = 0.1$; the dilute fill fraction means that $V_i \ll V_m$. Thus, a small volume change applied only to the inclusion causes a greater relative change to f than the same ΔV applied to only the matrix. On the left, $K_i \ll K_m$, so a fixed volume change in the composite affects the inclusion volume much more than the matrix, resulting in a high Δf and $|\gamma_{\text{art}}|$. On the right, the opposite is true, leading to a small Δf and $|\gamma_{\text{art}}|$. This is seen in Eq. (6), where for dilute f , the denominator becomes small when $K_i \ll K_m$, increasing the magnitude of the electrostriction. Supporting this argument is the

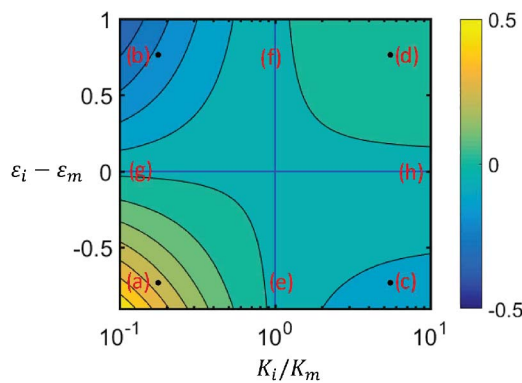


Fig. 4. Contour plot of γ_{art} versus $\epsilon_i - \epsilon_m$ and K_i/K_m with $\epsilon_m = 1$, $K_m = 1$, and $f = 0.1$. The permittivity axis is scaled linearly, whereas the bulk modulus axis is on a log scale. The surface is divided into quadrants (a)–(d) where lines (e)–(f) and (g)–(h) divide the quadrants.

fact that setting $f = 0.5$, so $V_i = V_m$, makes Fig. 4 left-right symmetric.

Second, the upper- and lower-half regions in Fig. 4, where $\epsilon_i > \epsilon_m$ and $\epsilon_i < \epsilon_m$, respectively, are approximately opposite. While this is not surprising since the permittivity contrast $\epsilon_m - \epsilon_i$ is the main driver for artificial electrostriction, the values on the upper half are slightly smaller in magnitude than the lower half. To explain this, we consider $\partial \epsilon_r^{\text{eff}} / \partial f = \partial \epsilon_{xx}^{\text{eff}} / \partial f$, which corresponds to the first bracketed factor in the last term in Eq. (6). We plot $\partial \epsilon_r^{\text{eff}} / \partial f = \partial \epsilon_{xx}^{\text{eff}} / \partial f$ versus $\epsilon_i - \epsilon_m$ (where $\epsilon_m = 1$ for numerical purposes), as shown by the red curve in Fig. 5. For $\epsilon_i - \epsilon_m < 0$, the dependence is almost linear, whereas for $\epsilon_i - \epsilon_m > 0$ it seems to saturate. To highlight the asymmetry between $\epsilon_i - \epsilon_m < 0$ and $\epsilon_i - \epsilon_m > 0$, we extend the horizontal axis to $\epsilon_i \gg \epsilon_m$. Figure 5 also shows $\partial \epsilon_{xx}^{\text{eff}} / \partial f$ for composites with different shape inclusions, and hence different g_x (see Fig. 3): $g_x = 1$ (blue solid curve) and $g_x = 0$ (blue dashed). Since symmetry is lost for non-spherical inclusions, we consider $\epsilon_{xx}^{\text{eff}}$ in place of ϵ_r^{eff} .

For $g_x = 0$, the inclusions are ideal needles oriented along x , and the effective permittivity is given by the well-known result $\epsilon_{xx}^{\text{eff}} = f\epsilon_i + (1-f)\epsilon_m$ [15]. Hence, $\partial \epsilon_{xx}^{\text{eff}} / \partial f = \epsilon_i - \epsilon_m$, which is unbounded. The inclusion and matrix permittivities add independently because the composite's substructure is in parallel with respect to x . In contrast, for $g_x = 1$, corresponding to the inclusions forming slabs normal to x , we have the equally well-known result $1/\epsilon_{xx}^{\text{eff}} = f/\epsilon_i + (1-f)/\epsilon_m$ [15]. Hence, $\partial \epsilon_{xx}^{\text{eff}} / \partial f = (\epsilon_i - \epsilon_m)(\epsilon_{xx}^{\text{eff}})^2 / (\epsilon_i \epsilon_m)$. If $\epsilon_i \gg \epsilon_m$, the strong depolarization field of the inclusion isolates the electric field from the matrix and nearly cancels the field in the inclusion because the composite's substructure is aligned in series with respect to x . Thus, in this limit, increasing ϵ_i only changes the permittivity in the region where the field is very weak, which has a minimal effect on $\epsilon_{xx}^{\text{eff}}$. Hence, $\partial \epsilon_{xx}^{\text{eff}} / \partial f \rightarrow 1/(1-f)^2$ for $g_x = 1$. The case of spherical inclusions ($g_x = 1/3$) lies somewhere between these two extreme inclusion geometries. At large fill fractions $\partial \epsilon_{xx}^{\text{eff}} / \partial f \approx 1/(g_x(1-f)^2)$ for all $g_x \neq 0$.

Finally, although Eq. (6) loses validity at high fill fractions, we now briefly investigate this regime. Increasing f tends to make Fig. 4 more left-right symmetric. This is because it reduces the

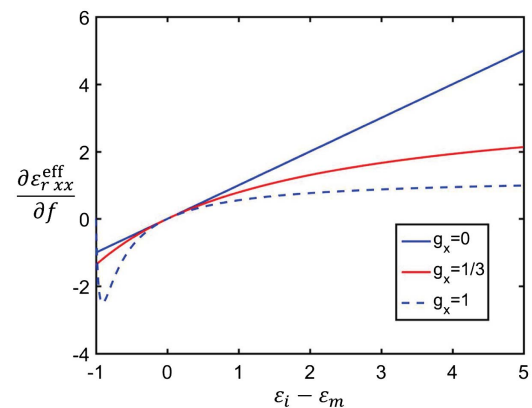


Fig. 5. $\partial \epsilon_{xx}^{\text{eff}} / \partial f$ for different g_x values, with $f = 0.1$. The spherical inclusion case ($g_x = 1/3$) lies in between the extremes $g_x = 0$ and $g_x = 1$.

imbalance in volume between inclusion and matrix. When $f = \frac{1}{2}$, the figure is symmetric about $K_i/K_m = 1$, and becomes more symmetric with respect to permittivity, although $\partial \epsilon_{xx}^{\text{eff}} / \partial f$ still approaches $1/(g_x(1-f)^2)$.

C. Electrostriction in Composites with Non-Zero Shear

When shear effects are included, the model in Section 2 fails, as changes to the shape of the matrix and the inclusion geometry cannot be ignored. Such phenomena are beyond analytic methods, and therefore a numerical method is required to calculate the electrostriction of solid–liquid and solid–solid composites. Using a commercially available finite element solver (COMSOL) and a procedure developed by Smith *et al.* [10] to investigate the effects of shear, we explain the behavior of artificial electrostriction in this more general setting. In our calculations we use unit cells of size 50 nm, which is deeply subwavelength at our optical wavelength of $\lambda = 1550$ nm.

Rather than determining each component of the electrostriction γ_{ijkl} , we need only compute γ_{xxyy} for most applications in optics, which applies to fields oscillating in a direction along the y -axis, generating compression waves in the orthogonal x -direction, as in SBS (Fig. 1). To determine $\gamma_{xxyy}^{\text{eff}}$ numerically, we first calculate the photoelastic tensor coefficient p_{xxyy} , which is related to the electrostriction tensor via [16]

$$\gamma_{xxyy} = (\epsilon_r^{\text{eff}})^2 p_{xxyy} \quad (7)$$

in materials of appropriate symmetry. The photoelastic tensor p_{ijkl} is a measure of how an imposed strain s_{kl} affects the inverse permittivity tensor:

$$\Delta(\epsilon^{-1})_{ij} = p_{ijkl} s_{kl}. \quad (8)$$

The numerical code works by calculating the effective permittivity of an unstrained unit cell, and the permittivity of a cell under a small strain applied in the y -direction. The photoelastic coefficient is then obtained by comparing the change in permittivity with the imposed strain, following Eq. (8). The effect of shear is quantified using the shear modulus $G = \sigma_{xy}/s_{xy}$, which is a measure of resistance to changes in shape [17]. The results of Section 2, which apply to $G_i = G_m = 0$, match the numerical calculations with $G_{i,m} \ll K_{i,m}$ well.

D. Numerical Results for Composites with Non-Zero Shear

In order to analyze the effect of shear, we consider a set of $(K_i, K_m, \epsilon_i, \epsilon_m)$ values from regions (a)–(f) in Fig. 4 and then expand the analysis to include shear. We again set $\gamma_i = \gamma_m = 0$ so that $\gamma_{xxyy} = \gamma_{\text{art}}$. In Fig. 6, particular results from each of the regions (a)–(f) in Fig. 4 are chosen for a composite, while G_i and G_m are varied. We do not include regions (g) and (h), where $\epsilon_i = \epsilon_m$, as the optical homogeneity results in $\gamma_{\text{art}} = 0$.

In Figs. 6(a)–6(f) the bottom left corners match closely the predictions of the zero-shear model of Section 2, as both shear moduli are much lower than the bulk moduli. Outside this region in Figs. 6(a)–6(d), G_m seems to have a significant scaling effect on the magnitude $|\gamma_{\text{art}}|$. In region (a), for example, increasing G_m lowers the electrostriction from 1.3 to 0.2, whereas in region (d) the scaling effect causes only a slight reduction in the electrostriction, since it is small to begin with. At first glance it

might seem that G_i has little impact on γ_{art} . However, overlaid on all plots (a)–(f) is a subtle additional dependence on shear: increasing G_m increases γ_{art} , while increasing G_i reduces γ_{art} (not $|\gamma_{\text{art}}|$). This is particularly noticeable in plots (e) and (f), but is present throughout Fig. 6. We now explain these observations.

Recall from Section 2.B that artificial electrostriction relies on a strain applied to a composite causing changes to the volume fractions of the matrix and of the inclusion. Changes to V_i must come from strains in the matrix, as the imposed strain is on the unit cell boundary. Now if the matrix has a shear modulus and is strained in only one direction, G_m suppresses the changes to V_m , and reduces deformations to the interior of the matrix, which in turn limits relative changes to V_i . Thus, G_m reduces artificial electrostriction. In contrast, including G_i has minimal impact on the fill fraction. The shear forces are applied to the outside of the unit cell, so that little shear force comes to the inclusion. Thus, changes to inclusion volume only weakly depend on its shear modulus, as the shear forces are minimal.

We now consider the more subtle observation that increasing G_m increases γ_{art} , while increasing G_i decreases γ_{art} (though not $|\gamma_{\text{art}}|$ if $\gamma_{\text{art}} < 0$). Such behavior is caused by changes to the shape of the inclusion, which alters its depolarization factor \mathbf{g} . Since changes to the shape are generally quite small, the magnitude of this effect is correspondingly small (~ 0.1), and is often outweighed by the principal effect discussed in the previous paragraph. Nevertheless, it gives important insight into the underlying physics.

To consider the effect of \mathbf{g} , we generalize the method of [11] to develop a Maxwell–Garnett model for the effective permittivity of a composite with general spheroidal inclusions in a cubic lattice [18]:

$$\epsilon_{xx}^{\text{eff}} = \frac{f\epsilon_i\epsilon_m + \epsilon_m(1-f)(g_x\epsilon_i + (1-g_x)\epsilon_m)}{f\epsilon_m + (1-f)(g_x\epsilon_i + (1-g_x)\epsilon_m)}. \quad (9)$$

To isolate the effect of \mathbf{g} , we take a first-order expansion in g_x :

$$\Delta\epsilon_{xx}^{\text{eff}} \approx -\frac{9\epsilon_m f(1-f)(\epsilon_i - \epsilon_m)^2}{[(1-f)\epsilon_i + (2+f)\epsilon_m]^2} \Delta g_x + O(\Delta g_x^2), \quad (10)$$

which shows that the $O(\Delta g_x)$ coefficient is always negative.

Straining the unit cell in the y -direction causes the sphere to stretch such that g_x increases, and hence by Eq. (10), we find that $\epsilon_{xx}^{\text{eff}}$ is reduced. Thus $\Delta(\epsilon^{-1})_{xx}$ is positive, as we assume the permittivity matrix to be diagonal. Relating this to shear effects, the imposed strain is along one principal axis, so either the matrix or the inclusion must change shape in response. When G_m is high, the matrix has a greater resistance to change in shape, so the inclusion is deformed in response to the strain. This increases g_x , making γ_{art} slightly more positive. On the other hand, increasing G_i reduces the inclusion's change in shape in response to the strain. Hence, by the same argument, increasing G_i reduces γ_{art} .

These effects completely explain the results presented in Fig. 6: Figs. 6(a)–6(c) have a high $|\gamma_{\text{art}}|$, so we largely observe that G_m suppresses $|\gamma_{\text{art}}|$, while G_i has a minimal effect on γ_{art} , apart from a small reduction as predicted by the change in the depolarization factor. In Fig. 6(d), where $|\gamma_{\text{art}}|$ is small, the changes in g_x more strongly affect artificial electrostriction, except at high G_m , where the scaling down of $|\gamma_{\text{art}}|$ dominates. Finally, Figs. 6(e) and 6(f) have no inhomogeneity in bulk

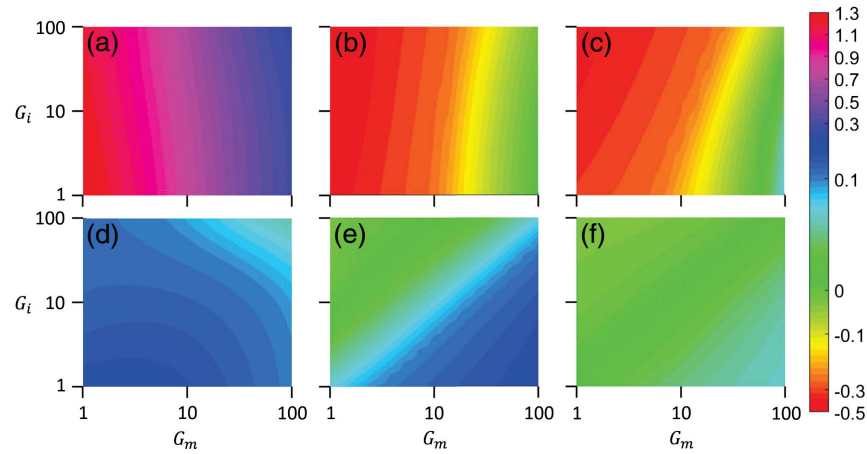


Fig. 6. Numerical results for γ_{art} versus G_i and G_m for various combinations of $(\epsilon_i, \epsilon_m, K_i, K_m)$ [GPa] where $f = 0.1$. References (a)–(f) correspond to particular points in regions (a)–(f) in Fig. 4 with exact values: (a) (1, 5, 10, 50); (b) (5, 1, 10, 50); (c) (1, 5, 50, 10); (d) (5, 1, 50, 10); (e) (1, 5, 10, 10); and (f) (5, 1, 10, 10).

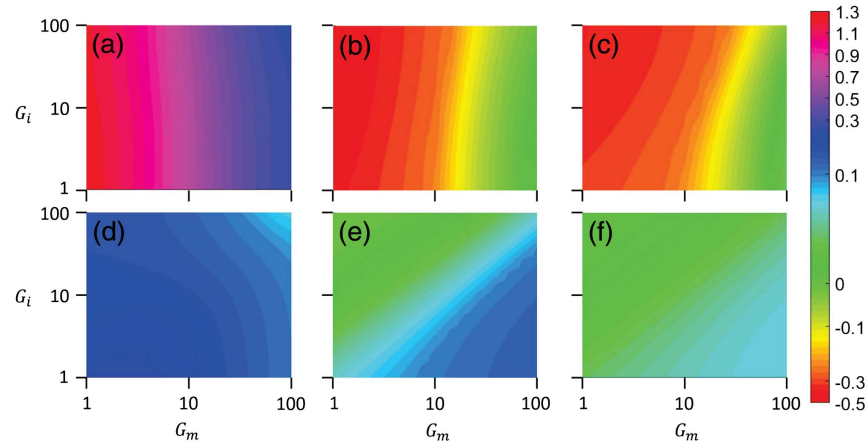


Fig. 7. Predicted γ_{art} versus G_i and G_m for various combinations of $\epsilon_i, \epsilon_m, K_i, K_m$ with $f = 0.1$. Regions (a) through (f) match the parameter sets in Fig. 6.

moduli, so shear effects are the only source of electrostriction. The trends seen in these graphs match those predicted by the depolarization factor effects in Eq. (9).

Figure 7 shows γ_{art} predicted by our model and can be directly compared with Fig. 6. It uses the intermediate step in the numerical method to obtain the strained geometry of a unit cell under a small imposed strain, and then Eq. (9) to predict the photoelastic term p_{xyxy} , and hence γ_{art} . The agreement with the full numerical calculation is excellent, with errors typically ~ 0.02 , in support of the model leading to Eq. (9).

3. RESULTS

The physical parameters K , G , ϵ_r , p_{xyxy} , and γ_{xyxy} for four relevant materials are given in Table 1. In Table 2 the top entries give the numerically calculated values for the artificial electrostriction for composites composed of these four materials, with $f = 0.1$. Comparing with the approximate result (not shown), we find that the discrepancies are less than 5%, consistent with

the results in Section 2.D. The bottom entries in Table 2 show the percentage contribution (in absolute value) of the artificial term to the overall composite electrostriction.

We begin by analyzing the magnitudes of the artificial term (top entries). The diagonal entries of Table 2 are identically zero as the inclusion and matrix materials are identical. For the off-diagonal terms, we note that the magnitude of the electrostriction is higher in the top-right part than on the bottom left of the table. This is because for small fill fractions f , the effect of $K_m > K_i$ is larger than when $K_i > K_m$ (see Section 2.B).

Table 1. Relevant Bulk Properties for Key Optical Materials

Material		K [GPa]	G [GPa]	ϵ_r	p_{xyxy}	γ_{xyxy}
As ₂ S ₃	[19]	10.4	6.4	5.6	0.24	7.53
SiO ₂	[20]	36.9	31.2	2.1	0.27	1.19
GaAs	[20]	93.1	59.6	11.4	−0.14	−18.19
Si	[20]	116.9	79.5	12.1	0.02	2.93

Table 2. Artificial Electrostriction of Different Composites^a

		Matrix Material			
		As ₂ S ₃	SiO ₂	GaAs	Si
Inclusion Material	As ₂ S ₃	0	−0.067	0.593	0.683
		0%	4%	5%	15%
	SiO ₂	−0.236	0	0.690	0.854
		3%	0%	5%	29%
	GaAs	0.344	0.190	0	0.010
		4%	15%	0%	6%
	Si	0.392	0.221	0.008	0
		5%	14%	0.1%	0%

^aTop entry: numerically calculated artificial electrostriction γ_{art} for various composites with $f = 0.1$ and including shear. Bottom entry: absolute value of percentage contribution of the artificial term to the overall composite electrostriction.

Even though the top-right cell of Table 2 (As₂S₃ spheres in Si) has the highest mechanical property contrast, it does not have the highest artificial electrostriction in the table. Rather, the cell below (SiO₂ spheres in Si) has the highest γ_{art} value, as its higher permittivity contrast makes up for the smaller mechanical difference. Moreover, the high G_m of silicon suppresses the stiffness contrast contribution to the electrostriction.

Composites made from As₂S₃ and SiO₂ have a negative artificial electrostriction because SiO₂ has a larger bulk modulus than As₂S₃, but SiO₂ possesses a lower permittivity than As₂S₃. Note that while the signs of the electrostrictions are symmetric about the diagonal since we are interchanging the permittivities and the mechanical properties simultaneously, the actual values are not symmetric.

Focusing now on the bottom entries in Table 2 we note that the artificial electrostriction varies between 5% and 30% of the composite's overall electrostriction, and hence can be quite substantial. The artificial electrostriction is modest in the GaAs and As₂S₃ columns in Table 2 because of the high constituent electrostrictions. However, in the SiO₂ column, the low permittivity leads to a low intrinsic electrostriction, so the artificial term contributes ~15% to the electrostriction. In the Si column, a very low inherent p_{xyy} means that the artificial term can contribute up to 30% of the overall electrostriction. This highlights how composites can be designed with significantly tuned electrostrictive properties by manipulating the artificial term, and identifies Si as a particularly promising material for this purpose.

4. DISCUSSION AND CONCLUSION

We have investigated artificial electrostriction including the effects of shear, to generalize our earlier investigations based only on hydrostatic responses. The model we have developed explains the origin and value of artificial electrostriction. While the model is semi-analytic in that it relies on a computational step to compute the strained geometry, it is a significant improvement on the previous analytic model, which does not include shear. From this model and from our numerical investigations, we find that the inclusion of shear effects tends to lower the artificial electrostriction, but that the magnitude of this effect can still contribute as much as 30% to the total electrostriction for weakly electrostrictive materials such as silicon. Since the strength of SBS depends

on $|\gamma_{\text{xyy}}|^2$ [10], a 30% increase in γ_{xyy} leads to a near doubling of the SBS strength, assuming, of course, that the other parameters are unchanged. The values of $|\gamma_{\text{art}}|$ can be significantly increased by taking a larger fill fraction of the inclusion—a doubling of f would lead by Eq. (6) to an approximate doubling of the artificial electrostriction. Another way to increase the artificial electrostriction is to use materials with larger contrasts in their mechanical properties.

Our numerical method produces reliable permittivity calculations, which we estimate to be reliable to four decimal places. Upon subtraction and division by imposed strain, errors come in to the third decimal place—this typically presents a random error of the order of 1% when numerical element sizes are varied. However, for low G_m , high G_i composites, the errors are somewhat more severe. While this could be improved by using a finer numerical grid, it would add significantly to the required computational effort.

The numerical method used to determine permittivities matches the Maxwell–Garnett model well, with errors <1%. This shows that the assumptions of a dilute inclusion and a homogeneous field are valid in this work, and in previous studies of SBS [10,21]. However, we did not investigate the impact of reducing the wavelength of the optical wave or increasing the fill fraction of the inclusion. We expect that the model presented here will lose validity as $f \gtrsim 0.2$ or as the wavelength becomes smaller with respect to the unit cell size.

This study opens pathways for investigation of electrostriction enhancement or suppression, and hence that of SBS, in metamaterials, showing how the electrostrictive properties of a composite can be changed by varying the material's geometric substructure. If a composite with small artificial electrostriction is required, then depolarization factor effects need to be taken into account. The artificial term is particularly significant in materials showing little inherent electrostriction.

Funding. Australian Research Council (ARC) (CE110001018).

Acknowledgment. We acknowledge financial support from the Australian Research Council (ARC) via the ARC Center of Excellence CUDOS.

REFERENCES

1. S. R. Anton, A. Erturk, and D. J. Inman, "Multifunctional self-charging structures using piezoceramics and thin-film batteries," *Smart Mater. Struct.* **19**, 115021 (2010).
2. B. M. Badr and W. G. Ali, "Applications of piezoelectric materials," *Adv. Mater. Res.* **189**, 3612–3620 (2011).
3. J. F. Nye, *Physical Properties of Crystals* (Oxford University, 1985).
4. R. E. Newnham, *Properties of Materials: Anisotropy, Symmetry, Structure* (Oxford University, 2005).
5. P. E. Powers, *Fundamentals of Nonlinear Optics* (CRC Press, 2011).
6. B. J. Eggleton, C. G. Poulton, and R. Pant, "Inducing and harnessing stimulated Brillouin scattering in photonic integrated circuits," *Adv. Opt. Photon.* **5**, 536–587 (2013).
7. E. Peral and A. Yariv, "Degradation of modulation and noise characteristics of semiconductor lasers after propagation in optical fiber due to a phase shift induced by stimulated Brillouin scattering," *IEEE J. Quantum Electron.* **35**, 1185–1195 (1999).

8. M. J. A. Smith, B. T. Kuhlmei, C. M. de Sterke, C. Wolff, M. Lapine, and C. G. Poulton, "Electrostriction enhancement in metamaterials," *Phys. Rev. B* **91**, 214102 (2015).
9. R. W. Boyd, *Nonlinear Optics*, 3rd ed. (Academic, 2003).
10. M. J. A. Smith, C. Wolff, C. M. de Sterke, M. Lapine, B. T. Kuhlmei, and C. G. Poulton, "Stimulated Brillouin scattering in metamaterials," *J. Opt. Soc. Am. B* **33**, 2162–2171 (2016).
11. L. Genzel and T. Martin, "Infrared absorption by surface phonons and surface plasmons in small crystals," *Surf. Sci.* **34**, 33–49 (1973).
12. V. A. Markel, "Introduction to the Maxwell Garnett approximation: tutorial," *J. Opt. Soc. Am. A* **33**, 1244–1256 (2016).
13. L. D. Landau, E. M. Lifshitz, and L. P. Pitaevskii, *Electrodynamics of Continuous Media* (Pergamon, 1960), Vol. 8.
14. A. Sihvola, "Dielectric polarization and particle shape effects," *J. Nanomater.* **2007**, 45090 (2007).
15. S. M. Rytov, "Electromagnetic properties of a finely stratified medium," *Sov. Phys. J. Exp. Theor. Phys.* **2**, 466–475 (1956).
16. P. T. Rakich, P. Davids, and Z. Wang, "Tailoring optical forces in waveguides through radiation pressure and electrostrictive forces," *Opt. Express* **18**, 14439–14453 (2010).
17. S. H. Crandall, N. C. Dahl, and T. J. Lardner, *An Introduction to the Mechanics of Solids*, 2nd ed. (McGraw-Hill, 1959).
18. G. W. Milton, *The Theory of Composites* (Cambridge University, 2002).
19. H. Ou, S. Dai, P. Zhang, Z. Liu, X. Wang, F. Chen, H. Xu, B. Luo, Y. Huang, and R. Wang, "Ultrabroad supercontinuum generated from a highly nonlinear Ge–Sb–Se fiber," *Opt. Lett.* **41**, 3201–3204 (2016).
20. M. J. Weber, *Handbook of Optical Materials* (CRC Press, 2002).
21. M. J. A. Smith, B. T. Kuhlmei, C. M. de Sterke, C. Wolff, M. Lapine, and C. G. Poulton, "Metamaterial control of stimulated Brillouin scattering," *Opt. Lett.* **41**, 2338–2341 (2016).